



# MIT Open Access Articles

## *Heazlewoodite, Ni<sub>3</sub>S<sub>2</sub>: A Potent Catalyst for Oxygen Reduction to Water under Benign Conditions*

The MIT Faculty has made this article openly available. **Please share** how this access benefits you. Your story matters.

<b>Citation</b>	Falkowski, Joseph M., Nolan M. Concannon, Bing Yan, and Yogesh Surendranath. "Heazlewoodite, Ni <sub>3</sub> S <sub>2</sub> #: A Potent Catalyst for Oxygen Reduction to Water Under Benign Conditions ." Journal of the American Chemical Society 137, no. 25 (July 2015): 7978–7981.
<b>As Published</b>	<a href="http://dx.doi.org/10.1021/jacs.5b03426">http://dx.doi.org/10.1021/jacs.5b03426</a>
<b>Publisher</b>	American Chemical Society (ACS)
<b>Version</b>	Author's final manuscript
<b>Citable link</b>	<a href="http://hdl.handle.net/1721.1/103926">http://hdl.handle.net/1721.1/103926</a>
<b>Terms of Use</b>	Article is made available in accordance with the publisher's policy and may be subject to US copyright law. Please refer to the publisher's site for terms of use.

# Heazlewoodite, $\text{Ni}_3\text{S}_2$ : a potent catalyst for oxygen reduction to water under benign conditions

Joseph M. Falkowski, Nolan M. Concannon, Bing Yan, Yogesh Surendranath\*

Department of Chemistry, Massachusetts Institute of Technology, 77 Massachusetts Avenue, Cambridge, Massachusetts 02139-4307, United States

## Supporting Information Placeholder

**ABSTRACT:** Electrodeposited thin films and nanoparticles of  $\text{Ni}_3\text{S}_2$  are highly active, poison and corrosion resistant catalysts for oxygen reduction to water at neutral pH. In pH 7 phosphate buffer,  $\text{Ni}_3\text{S}_2$  displays catalytic onset at 0.8 V vs the reversible hydrogen electrode, a Tafel slope of 109 mV/decade, and high Faradaic efficiency for four-electron reduction of  $\text{O}_2$  to water. Under these conditions, the activity and stability of  $\text{Ni}_3\text{S}_2$  exceeds that of polycrystalline platinum and manganese, nickel, and cobalt oxides illustrating the catalytic potential of pairing labile first row transition metal active sites with a more covalent sulfide host lattice.

The interconversion of water and  $\text{O}_2$  is an essential chemistry underlying a future renewable energy economy.<sup>1</sup> Nature executes this kinetically demanding multi-proton, multi-electron interconversion with remarkable selectivity and efficiency. Oxygen evolution is carried out at the  $\text{Mn}_4\text{Ca}$  cofactor of the oxygen evolving complex of photosystem II<sup>2</sup> whereas oxygen reduction is carried out at the heme/Cu active site of cytochrome C oxidase<sup>3</sup> and  $\text{Cu}_3$  cluster active sites of multicopper oxidases.<sup>4</sup> While these catalysts operate efficiently and selectively under benign conditions of neutral pH and ambient temperature and pressure, precious and base metal containing heterogeneous catalysts typically require highly alkaline or acidic electrolytes (Figure 1).

The paucity of heterogeneous electrocatalysts capable of efficient oxygen reduction at neutral pH<sup>5</sup> arises from two seemingly divergent kinetic/materials requirements: 1) the catalyst must remain active in the presence of buffering electrolytes that are required to maintain neutral pH stability and deliver protons to drive the proton-coupled electron transfer (PCET) activation of  $\text{O}_2$ <sup>6</sup> and 2) the catalyst must resist protolytic corrosion under reducing conditions. Precious metal catalysts such as Pt and Au meet the latter requirement but also strongly adsorb buffering electrolyte ions such as phosphate, degrading their catalytic efficiency.<sup>7</sup> In contrast, low valent mid to late first row transition metal ions are substitutionally labile,<sup>8</sup> allowing them to meet the first requirement, but this very property makes their corresponding oxides unstable with respect to corrosion in all but highly alkaline environments.<sup>9</sup>

Unlike metal oxides, bonding in transition metal sulfides is

more covalent, inhibiting their corrosion under similar conditions.<sup>10</sup> Thus, we envisioned that both of the above requirements could be met if a labile first row transition metal active site ion can be exposed at the surface of a sulfide host lattice. Here, we illustrate the effectiveness of this design strategy by uncovering a novel earth abundant catalyst for oxygen reduction at neutral pH, the heazlewoodite phase of nickel sulfide,  $\text{Ni}_3\text{S}_2$ . Under phosphate buffered neutral pH conditions,  $\text{Ni}_3\text{S}_2$  outperforms state of the art ORR catalysts including  $\text{MnO}_x$  and platinum owing to its unique combination of labile active sites and corrosion resistant sulfide lattice.

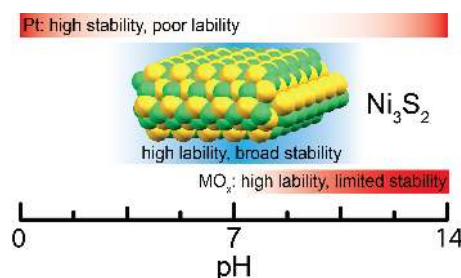


**Figure 1.** pH regimes of activity and stability for Pt, first row transition metal oxide ( $\text{MO}_x$ ), and  $\text{Ni}_3\text{S}_2$  ORR catalysts.

To probe accurately the specific catalytic activity of  $\text{Ni}_3\text{S}_2$ , we prepared conformal thin films on gold electrodes via layer-by-layer electrodeposition. The resulting films reflect the surface area of the underlying substrate allowing for straightforward comparisons between materials of different composition and phase. Adapting literature methods,<sup>11</sup> a planar polycrystalline gold electrode was exposed to 2.2 mM NaSH in 0.25 M  $(\text{NH}_4)_2\text{SO}_4$ , generating a spontaneous adlayer of sulfur.<sup>12</sup> To desorb excess sulfur from the adlayer, the electrode was subjected to controlled potential electrolysis at 0.03 V (all potentials are reported versus the reversible hydrogen electrode, RHE). Subsequent polarization of this sulfur-modified gold substrate in 10 mM borate electrolyte containing 5 mM  $\text{Ni}^{2+}$  resulted in the self-limiting deposition of a Ni adlayer. Repeated deposition cycles of sulfur and Ni following this same procedure give rise to thin films of nickel sulfide coating the gold electrode substrate.

To evaluate the nickel sulfide film morphology, we analyzed films prepared from 25 deposition cycles of Ni and S by cross

sectional SEM (Figure 2A). Field emission SEM images reveal the underlying Si wafer, Ti adhesion layer, and evaporated Au film in high contrast. On top of the Au layer, a 40 nm region of low contrast corresponding to the nickel sulfide thin film is observed. Importantly, the low contrast region exhibits uniform thickness across the sample with surface undulations that mirror that of the Au underlayer, indicating conformal growth of the nickel sulfide thin film.

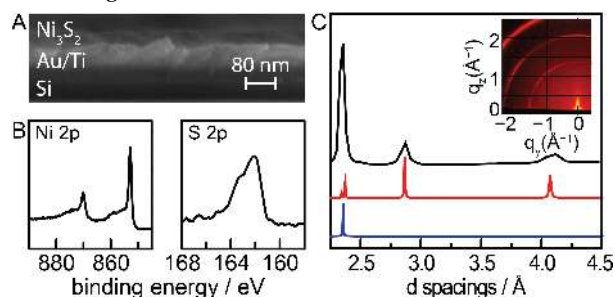


**Figure 2.** A) FE-SEM of a  $\text{Ni}_3\text{S}_2$  thin film prepared from 25 deposition cycles. B) High-resolution XPS spectra of the Ni 2p and S 2p regions of a  $\text{Ni}_3\text{S}_2$  film prepared from 10 deposition cycles following argon sputtering to remove adventitious surface oxides. C) Integration of grazing incidence X-ray diffraction data (inset) obtained on a  $\text{Ni}_3\text{S}_2$  thin film prepared from 50 deposition cycles (—). Simulated powder patterns for  $\text{Ni}_3\text{S}_2$  (—) and gold (—) are shown for comparison.

The electrodeposited films were analyzed by XPS and grazing incidence diffraction to probe their surface composition and phase. XPS analysis of the as deposited thin films (Figure S1) reveals three peaks in the Ni  $2p^{3/2}$  region at 861.4, 856.0 and 852.8 eV, and three peaks in the Ni  $2p^{1/2}$  region at 879.3 and 873.4, and 870.6 eV (Figure S2). Likewise, two peaks are observed in S 2p region of the XPS at 161.5 and 162.5 eV (Figure S2). Upon argon sputtering to remove the top surface layers of the film, the Ni 2p region collapses to a single set of peaks at 852.8 eV (Ni  $2p^{3/2}$ ) and 870.0 eV (Ni  $2p^{1/2}$ ) and the S 2p region collapses to a single peak at 162 eV (Figure 2B). Additionally, upon argon sputtering the O 1s peak intensity dramatically diminishes (Figure S3). Together, these observations are consistent with a thin surface oxide layer coating a uniform nickel sulfide thin film. Integration of Ni and S XPS peaks reveals a Ni:S ratio of  $\sim 3:2$  implying a  $\text{Ni}_3\text{S}_2$  empirical formula for the electrodeposited thin film.

To gain further insight into the structure of the electrodeposited thin film, we analyzed electrodes modified with 50 deposition cycles of Ni and S by synchrotron grazing incidence X-ray diffraction (Figure 2C). Three diffuse rings are observed across the detector area (Figure 2C, inset) consistent with a polycrystalline thin film that lacks significant preferred orientation on the gold substrate. Integration of the diffuse rings gives rise to a diffraction pattern with prominent peaks at 2.4, 2.9, and 4.1 Å d spacing (Figure 2C). These peaks correspond to the 003, 110, and 111 lattice planes respectively of the heazlewoodite phase of nickel sulfide ( $\text{Ni}_3\text{S}_2$ )<sup>13</sup> with overlapping diffraction from the Au 111 lattice plane of the underlying substrate at 2.4 Å d spacing. This data, taken together with the 3:2 ratio of Ni:S observed by XPS indicates that this deposition method generates conformal  $\text{Ni}_3\text{S}_2$  thin films.

As prepared, the electrodeposited  $\text{Ni}_3\text{S}_2$  thin films are highly active electrocatalysts for oxygen reduction to water at neutral pH. Slow scan (5 mV/s) linear sweep voltammograms of

a  $\text{Ni}_3\text{S}_2$  thin film prepared from 10 deposition cycles of Ni and S recorded in oxygen saturated, 1 M sodium phosphate, pH 7 (NaPi electrolyte) (Figure 3, —) reveals onset of catalysis at  $\sim 0.80$  V and gives rise to  $1 \text{ mA cm}^{-2}$  (all currents are normalized to the geometric surface area of the electrode) at  $\sim 0.61$  V, beyond which the catalytic current begins to plateau due to transport limitations. In the absence of  $\text{O}_2$ , only background double layer charging current is observed (Figure 3, —), indicating that the catalytic current is due solely to oxygen reduction mediated by the  $\text{Ni}_3\text{S}_2$  thin film.

Under these electrolyte conditions, the activity of  $\text{Ni}_3\text{S}_2$  exceeds that of other common precious and base metal oxygen reduction catalysts.  $\text{Ni}_3\text{S}_2$  films display catalytic onset  $\sim 0.1$  V more positive than both polycrystalline gold (Figure 3, —) and  $\text{Co}_9\text{S}_8$  thin films (—),<sup>15</sup> the latter viewed to be among the most active transition metal chalcogenide catalysts for oxygen reduction.<sup>16</sup> In neutral pH phosphate-buffered electrolyte,  $\text{Ni}_3\text{S}_2$  films also display superior activity relative to first row transition metal oxides commonly employed in alkaline media. Utilizing known anodic deposition protocols, thick, amorphous  $\text{NiO}_x$ ,<sup>17</sup>  $\text{MnO}_x$ ,<sup>18</sup> and  $\text{CoO}_x$ <sup>19</sup> films were prepared on gold substrates. Following annealing at 500 °C for 3 hours in air, the films were tested for ORR activity in  $\text{O}_2$  saturated NaPi electrolyte. LSV scans of  $\text{NiO}_x$  (Figure 3, —) and  $\text{MnO}_x$  (Figure 3, —) films reveal catalytic waves with onsets at  $\sim 0.7$  V, largely indistinguishable from the native activity of the Au substrate. Mn-oxide films also exhibit a reductive wave at 0.85 V prior to onset of ORR catalysis (Figure 3, —). This pre-wave is only observed on the first LSV scan of a freshly prepared  $\text{MnO}_x$  film and subsequent scans display features that are indistinguishable from the Au background (Figure S4). Based on the Pourbaix diagram of Mn in water,<sup>9</sup> we attribute the pre-wave to the reduction of  $\text{Mn}_2\text{O}_3$  to  $\text{Mn}^{2+}(\text{aq})$ . These results, coupled with the visible loss of both Mn and Ni oxide films from the electrode surface following CV cycling, indicate that these oxides rapidly corrode under reductive polarization in neutral phosphate electrolyte. In contrast, LSV scans of  $\text{CoO}_x$  films (Figure 3, —) reveal negligible initial ORR activity that improves slightly upon CV cycling (Figure S5), suggesting that this oxide is slightly more corrosion resistant but is nonetheless catalytically inert under these conditions.

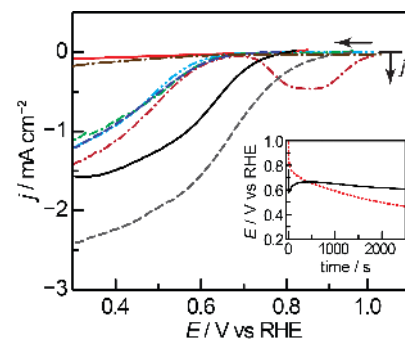


**Figure 3.** Linear sweep voltammograms of a  $\text{Ni}_3\text{S}_2$  thin film prepared from 10 deposition cycles (—), platinum (---), gold (•••),  $\text{MnO}_x$  (•••),  $\text{NiO}_x$  (•••),  $\text{CoO}_x$  (•••), and  $\text{Co}_9\text{S}_8$  (—) recorded at  $5 \text{ mV s}^{-1}$  in  $\text{O}_2$  saturated 1 M sodium phosphate electrolyte, pH 7. Linear sweep voltammogram of a  $\text{Ni}_3\text{S}_2$  thin film (—) in  $\text{N}_2$  saturated 1 M sodium phosphate electrolyte, pH 7. Inset: galvanostatic polarization traces at  $0.25 \text{ mA cm}^{-2}$  for a platinum (•••) and  $\text{Ni}_3\text{S}_2$  (—) electrode. All data recorded at 2000 rpm on a rotating disk electrode.

$\text{Ni}_3\text{S}_2$  films also outperform polycrystalline platinum under identical conditions. Initial slow scan linear sweep voltammograms of a polycrystalline platinum disk electrode reveals catalytic onset at  $\sim 0.90$  V, requiring  $\sim 0.1$  V lower overpotential than  $\text{Ni}_3\text{S}_2$  to catalyze ORR at comparable current densities. However, long-term electrolyses reveal that this enhanced activity is transient. Constant current polarization of a  $\text{Ni}_3\text{S}_2$  film at  $0.25 \text{ mA cm}^{-2}$  reveals a slight initial rise in activity following double layer charging after which the film carries out ORR catalysis at steady state reaching a potential of  $0.59$  V at the end of one hour (Figure 3 inset, —). In contrast, the potential required to maintain the same current density on Pt rapidly and progressively declines over the same time frame (Figure 3 inset,  $\bullet \bullet \bullet$ ). Within 10 minutes of polarization, the activity of polycrystalline platinum decays beyond that of  $\text{Ni}_3\text{S}_2$  and requires  $140$  mV more overpotential to sustain the same catalytic rate after 1 hour of constant electrolysis. This activity fade is also observed for high surface area Pt/C catalysts (Figure S6). In line with literature reports of strong phosphate adsorption to platinum surfaces<sup>7</sup> we attribute the decay of its ORR activity to progressive poisoning of the Pt surface by phosphate, a deactivation pathway that  $\text{Ni}_3\text{S}_2$  resists, allowing it to maintain high activity.

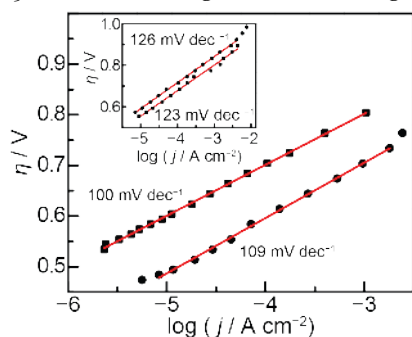


**Figure 4.** Applied overpotential versus steady state current density (Tafel plots) for ORR on  $\text{Ni}_3\text{S}_2$  ( $\bullet$ ) and  $\text{Co}_9\text{S}_8$  ( $\blacksquare$ ) thin film electrodes prepared from 10 deposition cycles. Data recorded in  $\text{O}_2$  saturated, 1 M sodium phosphate, pH 7, at 2000 rpm. Inset: Tafel plots of  $\text{Ni}_3\text{S}_2$  ( $\bullet$ ) and  $\text{Co}_9\text{S}_8$  ( $\blacksquare$ ) thin films recorded in  $\text{O}_2$  saturated, 0.1 M  $\text{HClO}_4$  at 2000 rpm.

Our observation of high ORR activity from  $\text{Ni}_3\text{S}_2$  contrasts previous literature reports suggesting that cobalt sulfides are superior catalysts relative to their nickel analogs.<sup>10,20</sup> To gain insight into the mechanistic basis for the opposite trend observed here, we constructed Tafel plots of overpotential versus the log of the activation-controlled current density for ORR (Figure 4) for thin films of  $\text{Ni}_3\text{S}_2$  and  $\text{Co}_9\text{S}_8$ , the latter viewed to be of the most active phase of cobalt sulfide.<sup>16</sup> At the higher overpotentials,  $\eta > 0.56$  V, the reaction proceeds under mixed activation and transport control and thus, we extrapolated Koutecky-Levich plots of reciprocal current density,  $j^{-1}$ , vs the reciprocal square root of the rotation rate,  $\omega^{-1/2}$ , to the y-axis, representing infinite rotation rate, to extract the activation controlled current density (representative Koutecky-Levich plots are shown in Figure S7).<sup>21</sup> The resulting Tafel plots (Figure 4) exhibit linear regions spanning 2.5 decades of current density and nearly  $0.3$  V in potential. Over this linear region, slopes of  $109$  and  $100 \text{ mV dec}^{-1}$  are observed for  $\text{Ni}_3\text{S}_2$  and  $\text{Co}_9\text{S}_8$  respectively, indicating that both proceed via rate-limiting 1-electron transfer to  $\text{O}_2$ .<sup>21</sup>

Despite a common mechanistic profile,  $\text{Ni}_3\text{S}_2$  outperforms

$\text{Co}_9\text{S}_8$  by  $\sim 1$  order of magnitude over the entire range of Tafel data collection at pH 7. In contrast,  $\text{Ni}_3\text{S}_2$  and  $\text{Co}_9\text{S}_8$  display similar activity in 0.1 M  $\text{HClO}_4$  (Figure 4, inset) and slightly higher Tafel slopes of  $126$  and  $123 \text{ mV dec}^{-1}$ , respectively, indicative of a common rate limiting one electron transfer step of catalysis with a slightly lower transfer coefficient,  $0.5$  at pH 1 vs  $0.6$  at pH 7. Thus, while  $\text{Co}_9\text{S}_8$  exhibits a nearly Nernstian pH dependence, giving rise to similar overpotentials independent of the electrolyte pH (Figure S8),  $\text{Ni}_3\text{S}_2$  exhibits a sub-Nernstian pH dependence, giving rise to higher activity as the pH increases (Figure S9). The precise origin of these divergent pH dependencies is the subject of ongoing investigations. Notwithstanding, these data indicate that  $\text{Ni}_3\text{S}_2$ 's superior activity at intermediate pH arises from a non-classical pH dependence on the reaction rate.

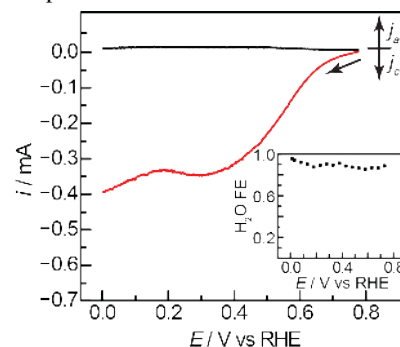


**Figure 5.** Rotating ring disk linear sweep voltammetry recorded at  $5 \text{ mV s}^{-1}$  in  $\text{O}_2$  saturated 1 M sodium phosphate electrolyte, pH 7. Disk current (—) for  $\text{O}_2$  reduction on a  $\text{Ni}_3\text{S}_2$  thin film prepared from 10 deposition cycles and ring current (—) for peroxide oxidation. Inset: Faradaic efficiency for  $\text{H}_2\text{O}$  production from  $\text{O}_2$  reduction.

To probe the selectivity of  $\text{Ni}_3\text{S}_2$  for direct 4-electron reduction of  $\text{O}_2$  to water we utilized rotating ring-disk electrode (RRDE) voltammetry. In this technique, oxygen is reduced at a rotating disk electrode modified with a  $\text{Ni}_3\text{S}_2$  thin film and any peroxide generated is oxidized back to  $\text{O}_2$  at a concentric Pt ring electrode allowing for direct quantification of the current efficiency for four-electron reduction of  $\text{O}_2$  to water. As seen in Figure 5, low currents are observed on the ring electrode over a wide potential range spanning the catalytic wave, corresponding to  $\sim 90\%$  faradaic efficiency for  $\text{O}_2$  reduction to water (Figure 5, inset).<sup>22</sup> This value is corroborated by the similarity in slopes of Koutecky-Levich plots of diffusion-limited currents for (Figure S10) of  $\text{Ni}_3\text{S}_2$  and Pt, a known 4-electron  $\text{O}_2$  reduction catalyst.<sup>23</sup>

The promising catalytic activity observed for  $\text{Ni}_3\text{S}_2$  thin films described above can be translated to nanoparticle systems. Nanocrystalline  $\text{Ni}_3\text{S}_2$  was prepared on Vulcan carbon XC-72R by refluxing a 1,5-pentanediol solution of  $\text{Ni}(\text{acac})_2$  and cystamine dihydrochloride in the presence of the Vulcan carbon support. The procedure generates  $10\text{-}50 \text{ nm}$   $\text{Ni}_3\text{S}_2$  nanoparticles dispersed on the carbon support with a minor NiS impurity phase that is known to be a poor catalyst for the ORR under these conditions.<sup>20a</sup> This carbon/ $\text{Ni}_3\text{S}_2$  composite, designated  $\text{Ni}_3\text{S}_2@\text{C}$ , was dispersed in ethanol, combined with a nafion binder and drop cast onto a glassy carbon rotating disk electrode at a  $\text{Ni}_3\text{S}_2$  loading of  $0.23 \text{ mg cm}^{-2}$  (see SI for details of catalyst loading determination). The composite film was tested for catalytic activity in  $\text{O}_2$  saturated, NaPi electrolyte (Figure 6). Consistent with the higher surface area

of Ni<sub>3</sub>S<sub>2</sub> in this carbon composite, current densities of 0.5 mA cm<sup>-2</sup> are observed at ~0.75 V, 85 mV lower overpotential than that required for Ni<sub>3</sub>S<sub>2</sub> thin films. Importantly, Ni-doped carbon composites prepared using identical synthetic conditions but with exclusion of the sulfur precursor display negligible activity (Figure S11) indicating that catalysis arises from Ni<sub>3</sub>S<sub>2</sub> rather than Ni-sites adsorbed on the carbon itself. The activity of the Ni<sub>3</sub>S<sub>2</sub>@C composite remains unchanged over the course of three hours of controlled potential electrolysis at 0.48 V, highlighting the stability of this material in phosphate buffered neutral pH electrolyte.

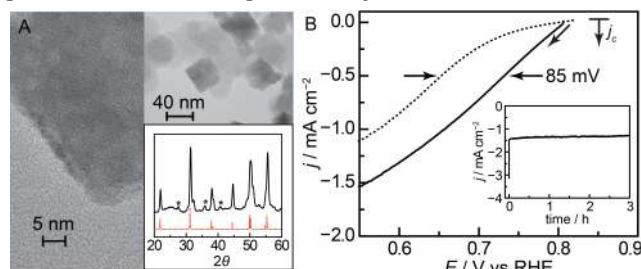


**Figure 6.** A. HR-TEM of Ni<sub>3</sub>S<sub>2</sub>@C. Inset: X-Ray diffraction pattern of the prepared Ni<sub>3</sub>S<sub>2</sub> (—) and a pattern simulated from literature data (---).<sup>13</sup> Stars denote a minor NiS impurity phase. B. Linear sweep voltammogram of a drop cast film of Ni<sub>3</sub>S<sub>2</sub>@C on a glassy carbon rotating disk electrode in O<sub>2</sub> saturated, 1 M sodium phosphate electrolyte, pH 7. The electrode was rotated at 2000 rpm. Inset: constant potential electrolysis Ni<sub>3</sub>S<sub>2</sub>@C at 0.48 V.

We have identified a new, highly active, earth-abundant oxygen reduction catalyst, Ni<sub>3</sub>S<sub>2</sub>, that operates effectively at neutral pH. Unlike first row transition metal oxides and Pt, Ni<sub>3</sub>S<sub>2</sub> resists corrosion and poisoning in phosphate buffered neutral pH electrolytes and its superior activity relative to Co<sub>9</sub>S<sub>8</sub> arises from a non-Nernstian pH dependence of oxygen reduction activity. These results, coupled with the observation of robust catalysis from carbon-supported Ni<sub>3</sub>S<sub>2</sub> nanoparticles, suggest that Ni<sub>3</sub>S<sub>2</sub> is an ideal candidate for oxygen reduction under intermediate pH conditions, potentially enabling the use of lower cost cell components and biological oxidation catalysts in functional devices.<sup>24</sup>

## ASSOCIATED CONTENT

### Supporting Information

Full experimental details, additional voltammograms, Koutecky-Levich plots, and XPS spectra. This material is available free of charge via the Internet at <http://pubs.acs.org>.

## AUTHOR INFORMATION

### Corresponding Author

Email: [yogi@mit.edu](mailto:yogi@mit.edu)

## ACKNOWLEDGMENTS

We gratefully acknowledge Sophie Liu, Anthony Hall, and Joe Strzalka for assistance with gold electrode fabrication, SEM data collection, and GIXD data collection, respectively. This research was supported by the Aramco Services Company through an MIT Energy Initiative Grant, the NSF under award CHE-1454060, and by the MIT Department of Chemistry through junior faculty funds for Y.S. This work made use of the MRSEC Shared Experimental Facilities at MIT, which

is supported in part by the NSF under award DMR-0819762.

## REFERENCES

- (1) (a) Katsounaros, I.; Cherevko, S.; Zeradjanin, A. R.; Mayrhofer, K. J. *Angew. Chemie Int. Ed.* **2014**, *53*, 102–121. (b) Lewis, N. S.; Nocera, D. G. *Proc. Natl. Acad. Sci. U. S. A.* **2006**, *103*, 15729–15735. (c) Gewirth, A. A.; Thorum, M. S. *Inorg. Chem.* **2010**, *49*, 3557–3566.
- (2) Umena, Y.; Kawakami, K.; Shen, J.-R.; Kamiya, N. *Nature* **2011**, *473*, 55–60.
- (3) (a) Ferguson-Miller, S.; Babcock, G. T. *Chem. Rev.* **1996**, *96*, 2889–2907. (b) Collman, J. P.; Devaraj, N. K.; Decréau, R. a; Yang, Y.; Yan, Y.-L.; Ebina, W.; Eberspacher, T. a; Chidsey, C. E. D. *Science* **2007**, *315*, 1565–1568.
- (4) Solomon, E. I.; Chen, P.; Metz, M.; Lee, S.-K.; Palmer, A. E. *Angew. Chemie Int. Ed.* **2001**, *40*, 4570–4590.
- (5) Wen, Z.; Ci, S.; Zhang, F.; Feng, X.; Cui, S.; Mao, S.; Luo, S.; He, Z.; Chen, J. *Adv. Mater.* **2012**, *24*, 1399–1404.
- (6) (a) Carver, C.; Matson, B.; Mayer, J. J. *Am. Chem. Soc.* **2012**, *134*, 5444–5447. (b) Rosenthal, J.; Nocera, D. G. *Acc. Chem. Res.* **2007**, *40*, 543–553.
- (7) (a) Wang, J. X.; Markovic, N. M.; Adzic, R. R. *J. Phys. Chem. B* **2004**, *108*, 4127–4133. (b) Li, Q.; Wu, G.; Cullen, D. a.; More, K. L.; Mack, N. H.; Chung, H.; Zelenay, P. *ACS Catal.* **2014**, *4*, 3193–3200. (c) He, Q.; Shyam, B.; Nishijima, M.; Ramaker, D.; Mukerjee, S. *J. Phys. Chem. C* **2013**, *117*, 4877–4887. (d) He, Q.; Yang, X.; Chen, W.; Mukerjee, S.; Koel, B.; Chen, S. *Phys. Chem. Chem. Phys.* **2010**, *12*, 12544–12555.
- (8) (a) Helm, L.; Merbach, A. E. *Chem. Rev.* **2005**, *105*, 1923–1959. (b) Taube, H. *Chem. Rev.* **1952**, *50*, 69–126.
- (9) Pourbaix, M. *Atlas of Electrochemical Equilibria in Aqueous Solutions*; National Association of Corrosion Engineers: Houston, Texas, 1974.
- (10) Bouroushian, M. *Electrochemistry of Metal Chalcogenides*; Springer-Verlag: Berlin, 2010.
- (11) Loglio, F.; Innocenti, M.; Jarek, A.; Caporali, S.; Pasquini, I.; Foresti, M. L. *J. Electroanal. Chem.* **2010**, *638*, 15–20.
- (12) Gregory, B. W.; Stickney, J. L. *J. Electroanal. Chem.* **1991**, *300*, 543–561.
- (13) Parise, J. B. *Acta Crystallogr. B* **1980**, *36*, 1179–1180.
- (14) Couderc, J. J.; Garigue, G.; Lafourcade, L.; Nguyen, Q. T. *Zeitschrift fuer Met.* **1959**, *50*, 708–716.
- (15) Falkowski, J.; Surendranath, Y. *ACS Catal.* **2015**, *5*, 3411–3416.
- (16) (a) Sidik, R. A.; Anderson, A. B. *J. Phys. Chem. B* **2006**, *110*, 936–941. (b) Melbourne, P. *Electroanal. Chem. Interfacial Electrochem.* **1975**, 151–162.
- (17) Bediako, D. K.; Lassalle-Kaiser, B.; Surendranath, Y.; Yano, J.; Yachandra, V. K.; Nocera, D. G. *J. Am. Chem. Soc.* **2012**, *134*, 6801–6809.
- (18) Huynh, M.; Bediako, D. K.; Nocera, D. G. *J. Am. Chem. Soc.* **2014**, *136*, 6002–6010.
- (19) Surendranath, Y.; Kanan, M. W.; Nocera, D. G. *J. Am. Chem. Soc.* **2010**, *132*, 16501–16509.
- (20) (a) Kishi, T.; Shimizu, F.; Nagai, T. *Surf. Technol.* **1984**, *21*, 109–115. (b) Iwaya, W.; Takase, S.; Shimizu, Y. *Electrochem. commun.* **2011**, *364*–366. (c) Zhu, L.; Susac, D.; Teo, M.; Wong, K.; Wong, P.; Parsons, R.; Bizzotto, D.; Mitchell, K.; Campbell, S. *J. Catal.* **2008**, *258*, 235–242.
- (21) Gileadi, E. *Physical Electrochemistry, Fundamentals, Techniques and Applications*; Wiley-VCH: Weinheim, 2011.
- (22) Albery, W. J.; Hitchman, M. L. *Ring-Disk Electrodes*; Oxford University Press: London, 1971.
- (23) Strbac, S. *Electrochim. Acta* **2011**, *56*, 1597–1604.
- (24) (a) Rismani-Yazdi, H.; Carver, S. M.; Christy, A. D.; Tuovinen, O. H. *J. Power Sources* **2008**, *180*, 683–694. (b) Yang, J.; Ghobadian, S.; Goodrich, P. J.; Montazami, R.; Hashemi, N. *Phys. Chem. Chem. Phys.* **2013**, *15*, 14147–14161. (c) Leech, D.; Kavanagh, P.; Schuhmann, W. *Electrochim. Acta* **2012**, *84*, 223–234.

Insert Table of Contents artwork here

